Stockholm Observatory

The Luminosity Function and Weak Lensing of the Galaxy Cluster Abell 2219

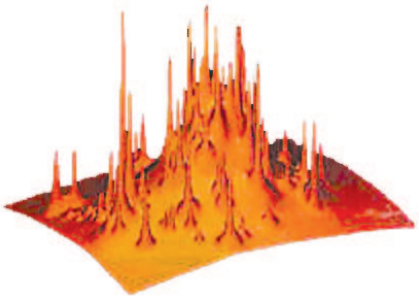

Sofia Ramstedt

Master Thesis

Dept. of Astronomy, Stockholm University

Stockholm 2003

Sofia Ramstedt: The Luminosity Function and Weak Lensing of the Galaxy Cluster Abell 2219

ABSTRACT

This diploma thesis contains the analysis of the rich galaxy cluster Abell 2219. Both the luminosity function and weak lensing are investigated using I-band CCD-images taken at NOT July 1999.

The luminosity function was determined using a statistical subtraction method. The result was $M_R^* = -22.6 \pm 0.1$ in absolute magnitude and $\alpha = -1.08^{+0.01}_{-0.10}$.

The weak lensing analysis resulted in a massmap of the cluster which is consistent with earlier results and shown in figure 2.7. The massmap is scaled in signal to noise.

Descriptors: Galaxy Cluster, Luminosity Function, Weak Lensing

Front page: A relief map of dark matter peaks around a cluster of distant galaxies.

Contents

1

Theoretical Background

Introduction

This thesis is a report on the analysis of a galaxy cluster, Abell 2219 (A2219), at z=0.225. I have studied the luminosity function (LF) and weak lensing of the cluster. The LF is defined as the number of galaxies in a certain luminosity range and a specific volume. Weak lensing is the gravitational bending of light coming from background sources, due to the assembled mass of the cluster. This kind of investigations can give us information about the evolution of galaxies and structure in the universe, the nature of dark matter, and by studying several clusters at different z, we learn about the structure and evolution of the universe.

Chapter 1 gives a short theoretical background. In chapter 2 I describe the observations, the analysis and the results. In chapter 3 I discuss the results and compare them with others. Finally chapter 4 contains a summary.

Throughout the thesis I have used $H_0 = 70$ Mpc km^{-1} s^{-1}, $\Omega_{\rm M} = 0.3$ and $\Omega_\Lambda = 0.7$, i. e. $\Omega_{\rm total} = 1$.

The magnitudes are Vega magnitudes.

1.1 Cosmology

New cosmological observations have been made and old ones have been confirmed during the last couple of years.

The recent WMAP measurement of the cosmic microwave background (CMB) confirmed earlier CMB measurements and showed that the universe has a flat geometry (k=0) and consists of 4 % baryonic matter, 23 % cold dark matter and 73 % dark energy. The new discovery made is that the expansion of the universe is accelerating.

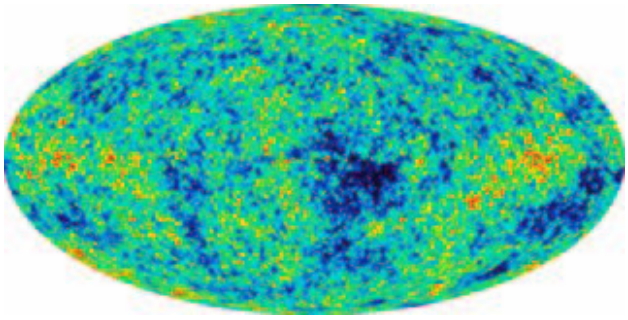

Figure 1.1: *The temperature fluctuations in the CMB as measured by WMAP.*

These observations help us to get closer to the answers to some fundamental questions on the Universe: What is its geometry? What does the universe consist of? How has the universe evolved so far and what will happen in the future? I will try, best I can, to give some of the conclusions made so far.

Measurements of the angular power spectrum of the CMB show multiple peaks and minima. These peaks arise due to the evolution of pressure waves in the early universe, before the decoupling of radiation and matter. Density inhomogeneities in the early universe, if they were large enough, were amplified after recombination, resulting in the formation of the structures we see in the universe today. Models of structure formation predict well-defined sets of peaks in the CMB spectrum with their relative position and amplitude for different values of the fundamental cosmological parameters. By comparing CMB measurements with these models, significant constraints can be put on for instance Ω_{total}; which is the total density of the universe (matter and energy) compared to the critical density, Ω_{b}; which is the baryon density, and Ω_{m}; which is the matter density. The critical density is the density the universe would have if the geometry is flat and the results from WMAP showed $\Omega_{\mathrm{total}} = 1.02 \pm 0.02$ ($\Omega_{\mathrm{m}}\mathrm{h}^2 = 0.135^{+0.008}_{-0.009}$ and $\Omega_{\mathrm{b}}\mathrm{h}^2 = 0.0224 \pm 0.0009$) (Bennett et al., 2003). The conclusion is that we live in a flat universe.

The acceleration of the expansion was observed by direct measurement of type Ia supernovae (SN Ia). SN Ia have nearly the same peak luminosity and any differences can be calibrated to 5 % in lookback time (Perlmutter & Linder, 2002). This means that comparing the redshift and magnitudes of different SN Ia shows

how the expansion of the universe has developed. The measurements were made by two groups using different techniques on different samples of high-z supernovae.

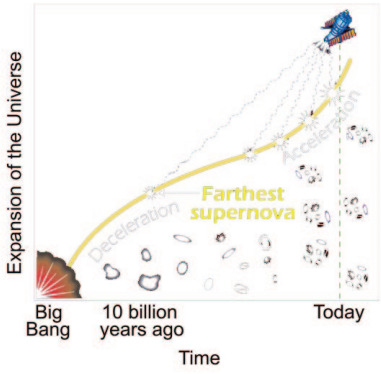

Figure 1.2: *Expansion of the universe.*

1.1.1 Dark Energy

WMAP and earlier measurements of the CMB anisotropy together with measurements of bulk flows and the baryonic fraction in clusters of galaxies show that matter only contributes about 1/3 of the critical density. This combined with the observed acceleration of the expansion has led to the suggestion of a new ingredient of the universe called dark energy. Dark energy has three defining properties: it emits no light, it has large negative pressure, comparable in magnitude to its energy density, and it is approximately homogeneous and does not cluster significantly with matter. In general relativity, both energy and pressure source the gravitational field. Sufficiently large negative pressure leads to repulsive gravity and this is why dark energy, as it is defined, explains accelerated expansion. The pressure imposed by the dark energy can be characterized by its equaton-of-state w. w is the ratio of the pressure to the energy density. w need not be constant, but for vacuum energy or the cosmological constant w=-1, for strings w=-1/3 and walls w=-2/3. Figure 1.3 shows confidence regions in the w-Ω_m-plane.

The dark energy must be very smoothly distributed, otherwise we would have observed its influence on matter and it must have been less important in the past in order not to interfere with the formation of structure by inhibiting the growth of density perturbations. Dark energy is the explanation of the acceleration of the universe and the missing part of the critical density. Suggested ways to detect it is to measure weak gravitational lensing by large-scale structure over very large fields (see section 1.4) (Turner, 2002), strong lensing of a number of lensing clusters at intermediate redshift (Serano, 2002) and supernovae surveys (Linder, SNAP Collaboration, 2002).

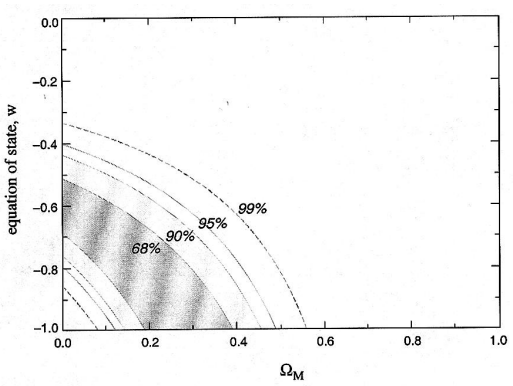

Figure 1.3: *Best-fit 68 %, 90 %, 95 % and 99 % confidence regions in the $\Omega_m - w$ plane for an additional energy density component, Ω_w, characterized by an equation-of-state ratio w=p/ρ. The fit shown is for a flat cosmology ($\Omega_m + \Omega_w = 1$).*

1.1.2 Dark Matter

The accumulations of baryonic matter represented by temperature fluctuations seen in the CMB could not have grown fast enough by themselves to collapse and form the large-scale structures that are common in the present universe. There must have been density fluctuations hundreds of times larger than these at the time of recombination, even though they do not show up today as temperature variations on the CMB.

Non-baryonic dark matter provides the solution. If the dark matter has a negligible interaction with radiation, it could have started to accumulate long before decoupling occured. After decoupling, baryonic matter would have been gravitationally attracted by already assembled clumps of dark matter.

Depending on the nature of the dark matter we get either a top-down formation process or a bottom-up. Hot dark matter (HDM), consisting of fast-moving particles, for instance neutrinos, tend to resist clumping due to diffusion. Any clumping that occur involves large amounts of mass, comparable to the mass of galactic clusters and superclusters and must be involved in a top-down process for forming galaxies from the breakup of larger quantities. If the stucture of the universe was formed in a top-down process we would see very few dwarf galaxies because they would not have had time to form yet. There are indications that this is not the case (Driver & Fernàndez-Soto, 1998; Tyson, 1988).

Instead the presently most popular theory of galaxy formation is hierachical clustering of cold dark matter haloes. Cold dark matter (CDM), slow moving particles, can begin to collect matter on a variety of scales when the matter era begins, forming haloes of different sizes. These haloes can then grow by accretion and mergers, resulting in a bottom-up scenario for forming galaxies from the assembling of smaller components. When the dark matter halo collapses, any gas admixed with it

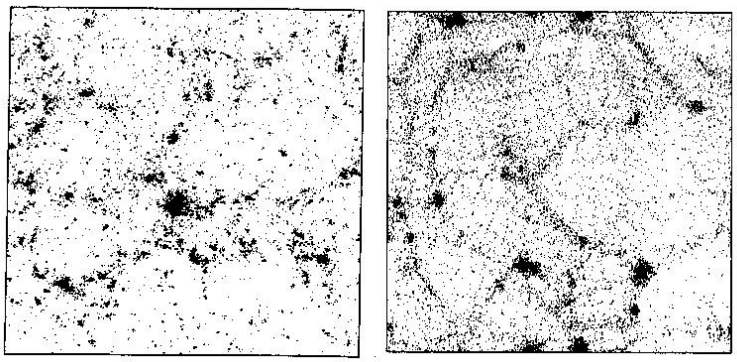

Figure 1.4: *The results of simulations of formation of structure. The left panel shows bottom-up clumping of CDM and the right, top-down fragmentation of HDM. (Figure from (Frenk et al., 1991)).*

will also collapse. By introducing the idea of feedback, where some of the gas is re-heated by an early generation of stars, the fact that not all the gas turned into stars could be explained. The details of star formation in the context of galaxy formation is not yet well understood (Frenk et al., 1996). N-body simulations (Colberg et al., 2000) studying two different CDM models was consistent with the CMB-fluctuation amplitude measured by COBE and with the observed abundance of rich clusters at z=0 (White & Frenk, 1991).

When investigating clusters of galaxies we see indications of the presence of dark matter.

Historically, cluster masses have been derived using the virial theorem. If the cluster is in virial equilibrium, we can, by measuring the velocity dispersion and the radius of the cluster, calculate the total dynamical mass of the cluster. To do this it is necessary to derive an expression for the gravitational potential energy of the cluster. For a spherical mass distribution, assuming that the density is constant and equal to the average value, the virial mass of a cluster is given by

$$M_{virial} = \frac{5R\sigma_r^2}{G}, \tag{1.1}$$

where R is the cluster radius and σ_r is the radial component of the velocity dispersion. These investigations showed a large M/L ratio, which indicates that the clusters contain more matter than we see. One component of the non-luminous matter is the X-ray emitting gas that is present in clusters, but still the stars and the gas only accounts for less than half of the gravitational mass.

The problem with using the virial theorem is that we can not always be sure that it applies, i. e. that the cluster really is fully relaxed. Also, the virial theorem only gives the total mass. A different way of investigating the gravitational mass of a cluster is to look at how much it bends the light of background sources; gravitational

lensing. Gravitational lensing can also give us the distribution of mass within the cluster. This will be described in section 1.4.

Another indication of dark matter, on a smaller scale, is the rotation curves of galaxies. A rotation curve shows the rotation velocity of a galaxy at different radii. In the outer parts of a galaxy, outside most of the visible matter, one should expect the velocity to decrease as $r^{-1/2}$ as in the solar system, where most of the mass is concentrated in the center. Investigations show that in most cases it does not. Instead the rotational velocity stays nearly constant out to large radii. One of the early results of N-body simulations was that the rotation curves of dark galactic haloes in the standard CDM model are flat (Frenk et al., 1996) giving a way to explain that the rotational speed in spiral galaxies does not decrease with radius.

The dark matter is present and can be seen by its gravitational influense on its luminous surroundings on different scales in the universe. The next section will descibe the luminous structures of the universe.

1.2 The Large Scale Structure of the Universe

1.2.1 Structure

As a consequence of the formation processes described above, the galaxies are not uniformely spread over the universe. The CfA (Center for Astrophysics) redshift surveys, reaching out to 15000 km s^{-1}, first showed that the universe contains voids with no or few galaxies and, in between the voids, filaments with galaxies (Huchra et al., 1990). Slices from the CfA survey show that galaxies form the walls of bubble-shaped regions, while inside the bubbles there are huge voids. Other redshift surveys done since then show the same thing (Figure 1.5).

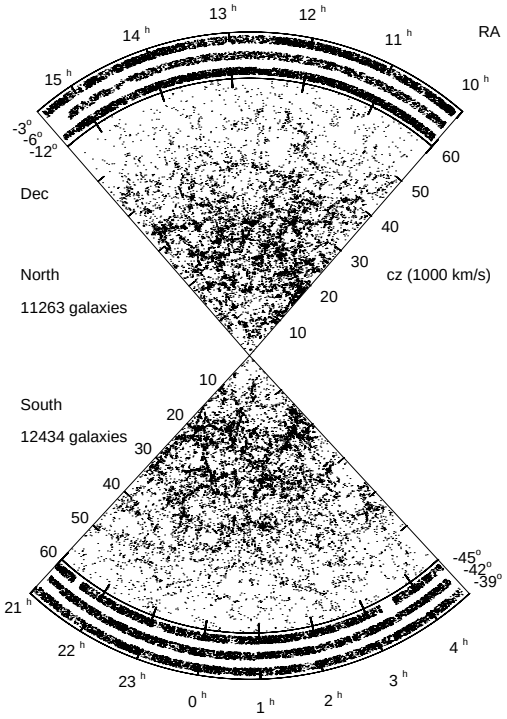

Figure 1.5: *The Las Campanas Redshift Survey consists of 26418 galaxies (Lin et al., 1996).*

At the intersection of these bubbles rich clusters of galaxies and super-clusters are found. The galaxies are divided into field galaxies and galaxies that belong to a gravitationally bound system, a group or a cluster.

The main difference between a group and a cluster is the number of galaxies it contains. The definition most often used is that a group consists of less than 50 galaxies, while a cluster contains thousands. For example, the Local Group, with the Milky Way, consists of 28 galaxies ($M_B \leq -8$) (Binney & Tremaine, 1987), while my investigation of the cluster A2219 showed 102 galaxies ($M_B \leq -19.5$), just within a radius of 0.5 Mpc. If the same magnitude limit is used for the Local Group, as for A2219, only two galaxies are visible. This results in other differences. For instance, the velocity dispersion varies with size and is therefore larger in a cluster than in a group. Typical estimates are 800 km s^{-1} in a cluster and 150 km s^{-1} in a group (Binney & Tremaine, 1987). These values are, of course, different for different clusters (see table 3.2) and different groups. The large clusters have velocity dispersions well over 1000 km s^{-1}.

Dense clusters have a radial morphological gradient, i. e. the different galaxy types vary from the inner part of the cluster to the outer regions. Elliptical galaxies are more common in the center, often with a big cD galaxy near the center of the cluster, perhaps at the bottom of the clusters gravitational potential well (Dubinski, 1998). Spirals and dwarfs are dominating the outer parts.

Although a subject of controversy, morphological studies also show that the number of ellipticals decreases backwards in time (see Diaferio et al. (2001) and ref. therein). In contrast, the number of faint galaxies has been seen to increase with redshift.

Also a radial color gradient is expected. The accretion of gas-rich field galaxies gives rise to new blue star-forming galaxies in the outerparts of clusters. Butcher and Oemler found that irregular or less concentrated clusters have higher fraction of blue galaxies, f_B, than compact clusters at the same redshift. This suggests that the internal structure of the cluster affects the blue fraction.

Butcher and Oemler also found that f_B increases dramatically between z=0 and $z \sim 0.5$. This is called the Butcher Oemler effect and is explained by the higher rate of star formation in cluster galaxies at earlier epochs. The reason for it is however not fully understood.

Luminosity distribution studies of seven rich galaxy clusters at z=0.15 (Driver et al., 1998) showed a dwarf-to-giant ratio distribution of 0.8-3.1. Different properties, density and environment of specific clusters play an important role in the evolution of a cluster (Phillipps et al., 1998) and caution should be taken in making conclusions about galaxy cluster evolution from a few observations at different z.

1.2.2 Evolution

Several processes are thought to govern the evolution of galaxies within a cluster. Due to the large value of the velocity dispersion in clusters, encounters between galaxies occur frequently and rapidly. These encounters can dramatically change the morphology and gas content of the galaxies involved.

One widely accepted view is that spiral galaxies can merge to form elliptical galaxies. The time scale of galactic merger makes it impossible for us to directly observe two galaxies merging, so how do we know that they do merge? Observations supporting this are for instance that ellipticals are more common in dense

environments, where collisions occur more frequently. Also, central regions of many ellipticals have more than one core and ripples and faint arcs observed inside elliptical galaxies are thought to be an indication that these galaxies are merger remnants (Schweizer, 1986). If elliptical galaxies are less common at larger z and faint galaxies are more common, as mentioned above, this would perhaps be an indication that the fainter galaxies have merged and formed larger elliptcals. Ongoing merger and collisions can be observed in the sky (Figure 1.6).

One feature of the elliptical galaxies are their very low gas content compared to spirals. This could also be explained by the collision scenario, as collisions and encounters can initiate star formation. Some of the gas from the initial spirals would build the stars and the rest would be blown away by the supernovae explosions. Or the gas could have been tidally stripped.

Dynamical friction can get very strong when two galaxies overlap during a close encounter. But even at seperations of a few diameters, galaxies induce tidal deformations on each other that cost them orbital energy. Tidal forces can also dissipate the orbital energy by pulling stars and gas out of one or both galaxies. This is called tidal stripping. Instead of pulling stars and gas out of the galaxies, tidal forces can induce starbursts. IRAS detected new galaxies with extraordinarily high rates of star formation. In interacting galaxies, supersonic collisions of gas could have triggered gigantic starbursts (Schweizer, 1986) (figure 1.6, again).

Alar and Juri Toomre (Toomre & Toomre, 1972) did calculations with a simple gravitational model, colliding two disks of non-interacting test particles revolving around a central mass, and were able to explain bridges and tails (Figure 1.6) observed as results of close encounters. They also suggested that inelastic collisions would lead to galaxy mergers. This led to further investigations and today computer simulations where two spirals merged into an elliptical galaxy have been done. Barnes and Hernquist (1996) simulated collisions between equal-mass disk galaxies, including gas dynamics, and found that the gas plays an important role. Tidal forces during encounters cause otherwise stable disks to develop bars and the gas flows toward the central regions were it may fuel starbursts. Barnes and Hernquist suggest that these stars could be detectable in real merger products by investigating the difference in age and metallicity of the stars in a galaxy. So far not much work has been done simulating close encounters including gas due to the very large number of particles these simulations have to include.

Moore et al. (1999) followed the evolution of disk galaxies within a cluster in a cold dark matter N-body simulation and observed galaxy harassment of low surface brightness (LSB) galaxies. LSB galaxies, characterized by slowly rising rotation curves and large scale lengths, evolved dramatically under the influence of rapid encounters and strong tidal shocks from the global cluster potential. 90 % of the stars of the LSB were tidally stripped and the bound stellar remnants resembled dwarf spheroidals.

N-body simulations investigating the origin of the giant elliptical galaxies in cluster centers showed that the central galaxy forms through merger of several massive galaxies early in the clusters history. Galactic cannibalism of smaller galaxies over a Hubble time are also involved in the evolution of the giant elliptical, but only accounts for a small fraction of the galaxies accreted mass (Dubinski, 1998).

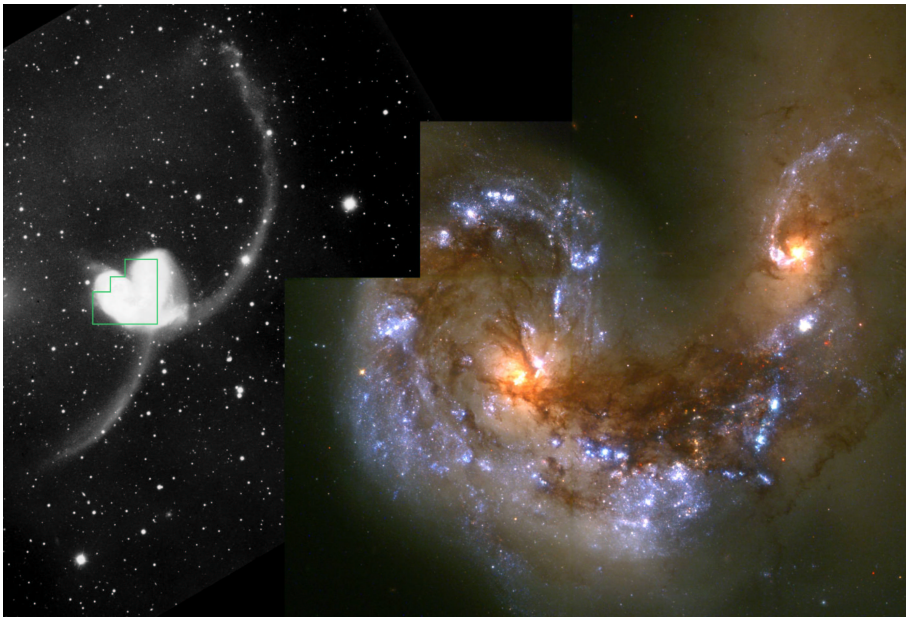

Figure 1.6: *An example of starformation in interacting galaxies. The blue star-clusters in the HST image (right) of NGC 4038 and NGC 4039 show how their recent collision has triggered starformation throughout both galaxies. The left image is taken with a ground-based telescope and shows the tails of the same galaxy pair (HST, 1997).*

There is an ongoing debate about what processes govern the formation and evolution of galaxies. Most agree that galaxies do collide and merge and at least some ellipticals are formed through disk mergers and many more have accreted luminous matter.

1.3 The Luminosity Function

The distribution of galaxies is characterized by the luminosity function (LF), defined as the number of galaxies δN in a certain range of luminosity δL and in a specific volume δV,

$$\Phi(L) = \frac{\delta N}{\delta L \delta V}. \tag{1.2}$$

It is closely related to the galaxy mass function, which is an important parameter in galaxy formation models. By comparing the LF for different clusters we can study the evolution of galaxy clusters. The LFs for fields, areas without clusters, are also interesting to study, for example, to get a picture of the distribution of different galaxy types in areas with varying galaxy density.

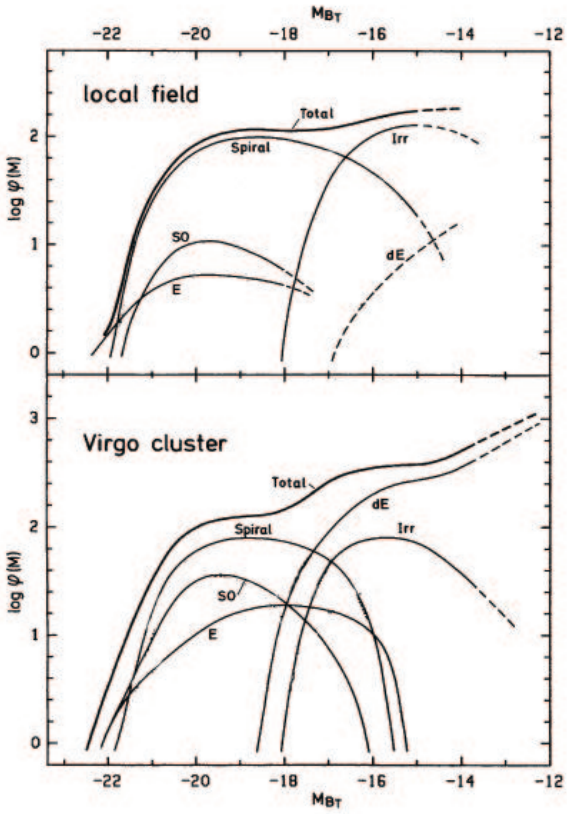

Figure 1.7: *The luminosity function showing different galaxy types (Binggeli et al., 1988).*

Figure 1.7 (Binggeli et al., 1988) shows that the LF are different for the field and for the Virgo cluster and that the total LF is a sum of single mostly bell-shaped

curves. Spirals dominate the luminous end together with ellipticals and SO galaxies, while the faint end is dominated by irregulars and dwarf galaxies. The upper plot shows the LF of the local field and the lower shows the LF of the Virgo cluster. It also shows a difference in the faint end slopes of the total LF of the field and of the Virgo cluster. Since figure 1.7 shows the local field, the distances to the different galaxies are known and the absolute magnitudes can be calculated. However, the field LF is much more uncertain, than the LF of the Virgo cluster, since it is based on a much smaller number of galaxies. When using the background subtraction method to obtain the LF of a cluster, as in sections 2.4 and 3.1, the magnitudes of the field galaxies are calculated from the redshift of the cluster, since they are subtracted from the cluster image. Different LF:s apply to different morphological types and the LF, summed over all types, depends on the environmental density.

Different cosmological models result in different LFs. The slope at the faint end is especially interesting, since the number of faint galaxies seen today is a clear indication of whether the stuctures of the universe were formed with a top-down or a bottom-up process as mentioned in section 1.1.

J. S. Heyl et al. (1995) tried to predict the observable properties of the galaxy population in several hierachical models of galaxy formation, contrasting the standard CDM model, and used the LF to evaluate the success of their results, comparing the different models to a LF made to fit observations. To get the best possible fit for each model, they had to choose an appropriate value for the stellar mass-to-light ratio, since this effects the turn-off point at bright magnitudes. The bright end is influenced by the choice of merger rate parameters, since mergers, of course, produces brighter galaxies and star formation rates and feedback, which have effects on the faint-end slope of the LF, when constructing a cluster. They found that none of the tested models produced broad agreement with observations.

When considering these matters it is important to seperate the formation of the dark matter halo from the formation of stars within the halo. The LF gives the distribution of luminous matter and the galaxy mass function gives both dark and luminous matter. According to CDM hierachical clustering model there should be numerous low-mass dark haloes. Small systems form earlier, and merge into larger units as time passes, but many low-mass haloes survive. The logarithmic slope of the low-mass end of the galaxy mass function is close to -1.8 (Trentham & Tully, 2002). Trentham & Tully (2002) conclude that if CDM theory is correct, the formation of stars in low-mass dark haloes is subject to disruption. Based on their observations of five different environments of varying galaxy density and morphological content they suggest that the anticipated mass function is steeper than the observed LF in any environment. Figure 1.8 shows six different LFs for clusters with different crossing times. If the crossing time is short, the galaxies in the cluster have undergone many interactions. A least squares linear fit to the average LF for the six, resulted in a faint end slope $\alpha = -1.19 \pm 0.03$, which is much flatter than the galaxy mass function and thus indicates a lack of luminous matter.

Tully et al. (2002) investigate observations of four different clusters and concludes that there is an absence of dwarf galaxies at least in low-density regions. They suggests that a plausible explanasion for the apparent lack of dwarf galaxies

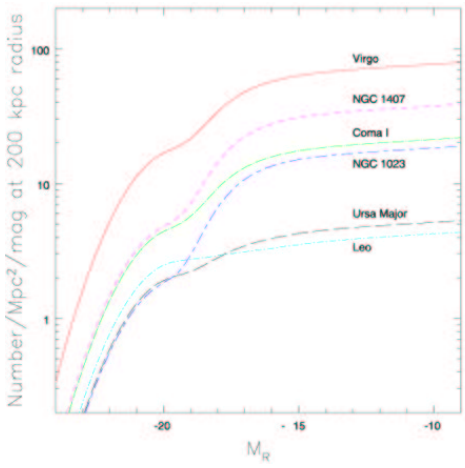

Figure 1.8: *Six LFs from clusters with different galaxy density. Listed in decreasing order of number of dwarfs per Mpc^2 the clusters are: the Virgo cluster, the NGC1407 group, Coma I, a group of galaxies in the Coma cluster, the Leo group, the NGC 1023 group and the Ursa Major cluster. The LFs are shallower at the faint end than the galaxy mass function predicted by CDM models.*

is photoionization of the intergalactic medium at a time before the formation of dwarf galaxies in low-density regions, but after the epoch of formation of similar systems that end up in rich clusters. The UV flux causing the reionization originates from young galaxies and quasars. Dynamical collapse times inferred from the observed densities of clusters are consistent with that relatively more dwarfs haloes formed before reionization in high-density regions, but only if structure is forming at high redshift, i.e., $\Omega_{\rm M} \leq 0.4$ (see section 1.1) in a flat universe.

Low mass galaxies are formed in large numbers in hierachical clustering scenarios and generally they are expected to form at high redshifts. Babul and Rees (1992) suggest that the dwarf elliptical (dE) galaxies formed relatively recently ($z \leq 1$) and that the faint blue objects seen in deep images in the sky are dwarf galaxies undergoing their first burst of star formation. The increase in the starburst activity in low-mass haloes is correlated with the decline in the UV background in the universe. When the flux declines the gas in the haloes can cool, collapse and undergo star formation. Babul and Rees suggests that the dE populations seen in clusters were initially in an environment where the external medium inhibited the massflow so that the dwarf galaxies could retain a greater fraction of gas and form more stars. Whereas gas in a less dense environment, where the local intergalactic medium pressure is smaller, was expelled from the galaxies by supernovae. These galaxies have faded and are difficult to detect today. However, Tully et al. (2002) found four small groups containing only dwarf galaxies. Dynamical investigations showed that these groups contained large amounts of dark matter, suggesting that a significant fraction of the group mass is made up of low-mass haloes that never

hosted significant star formation.

These investigations were continued and in 1996 Babul and Ferguson show that the local LF predicted by their model, with recent dwarf galaxy formation, has a very steep end at magnitudes fainter than $M_B = -16$. They also compare their model with some observations that also show a steep faint end of the LF (see references in Babul & Ferguson (1996)). At least one of these observations is of rich clusters of galaxies, so it does not necessarily contradict the results of Tully et al..

Schechter (1976) found an analytic expression for the LF, which is now widely used. Expressed in magnitudes M the Schechter function is

$$\Phi(M) \propto e^{-10^{0.4(M^*-M)}} \cdot 10^{-0.4(\alpha+1)M}, \tag{1.3}$$

where M^* represents the turnoff at bright magnitudes and α is a measure of the slope of the faint end. The function often gives a good fit to the data, even though recent deep measurements of the LF show that more complicated expressions are needed in order to give a satisfactory fit. Dahlén et al. (2002) used photometric redshifts to investigate the galaxy population of intermediate redshift clusters ($z \sim 0.5$) and found no evidence of a universal shape of the total LF. The LF for the early-type galaxies in the clusters can be described by a Gaussian, and a Schechter function is well fitted for the late-type galaxies. Trentham et al. also use a combination of a Gaussian and a Schechter function to fit their data from the Virgo cluster.

Christlein & Zabludoff (2003) investigated the LFs of six nearby galaxy clusters with different velocity dispersions resulting in composite LFs for cluster and field. The composite LFs were consistent with single Schechter functions.

Although the LF is rather straightforward to measure there are difficulties associated with attaining it. One of the biggest obstacles is to seperate the galaxies belonging to the group to be investigated, from the background and foreground galaxies, especially if you are interrested in the faint end. As pointed out by Trentham et al. (2002), spectroscopic redshifts are difficult to obtain for all but the nearest low-luminosity galaxies, since distances and hence luminosities are difficult to establish because of low surface brightness. A second problem is large Poisson counting errors due to that low-luminosity galaxies are rare in any magnitude-limited sample relative to more luminous background galaxies. Thirdly, very rich clusters, where Poisson statistics are manageble, are too far away for very faint galaxies to be unambiguously identified as cluster galaxies.

These difficulties, both observational and analytical results in uncertenties in the value of for instance α for different clusters and when looking at different investigations of the same cluster there are differences in faint end slope as well as the rest of the LF (see Figure 10 in Trentham (1998)).

1.4 Gravitational Lensing

Gravitational lensing was predicted already by Einstein, and in 1979 the first lens was discovered. The idea is to use the fact that lightrays are deflected in a gravitational field. When a lightray passes a pointmass it is deflected by

$$\alpha = \frac{4GM}{c^2 \xi}, \tag{1.4}$$

where ξ is the impact parameter. This formula can be used to estimate the gravitational mass of a cluster.

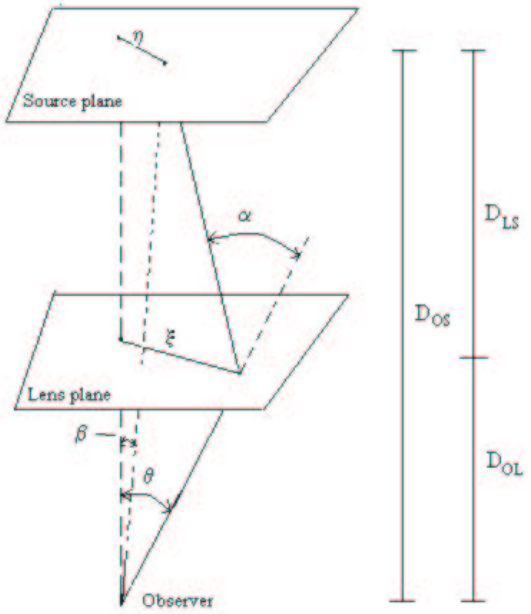

Figure 1.9: *A figure showing the different parameters used in the equations.*

A more accurate formula for the deflection angle of a lens/cluster is given in equation 1.5 (Bartelmann & Schneider, 1999) where the deflection angle depends on the projected mass density of the lens and on the cosmological parameters through

the angular diameter distances, defined by $\eta = \mathrm{D_{OS}}\beta$ and $\xi = \mathrm{D_{OL}}\theta$.

$$\alpha(\theta) = \frac{4GM}{c^2} \cdot D_{OL} \frac{1}{\pi} \int \Sigma(\theta) \frac{\theta - \theta'}{|\theta - \theta'|^2} d^2\theta' \tag{1.5}$$

where θ is the apparent angular position of the lensed image, D_{OL} is the angular diameter distance from the observer to the lens and $\Sigma(\theta)$ is the projected mass density of the lens. θ can be expressed in terms of the unlensed angular position of the source, β, and the angular diameter distances from the lens to the source, $\mathrm{D_{LS}}$, from the observer to the source, $\mathrm{D_{OS}}$, and the deflection angle, α.

$$\theta = \beta + \frac{D_{LS}}{D_{OS}} \alpha(\theta) \tag{1.6}$$

In general, equation 1.6 has more than one solution, illustrating the fact that lenses can produce multiple images.

A critical case occurs when $\theta = 0$, that is when there is a perfect alignment between the observer, the lens and the source. The lensing will result in a strongly magnified ring at the Einstein radius θ_{E}.

$$\theta_E = \left[\frac{4GM}{c^2} \frac{D_{LS}}{D_{OL} D_{OS}} \right]^{1/2} \tag{1.7}$$

In the case of perfect alignment between the cluster and the background source the lensing will result in a ring, but in most cases the result is in a number of arcs. Some of these arcs can be seen in A2219. A more beautiful example can be seen in the Hubble Space Telescope image of CL0024+1654 (see figure 3.6).

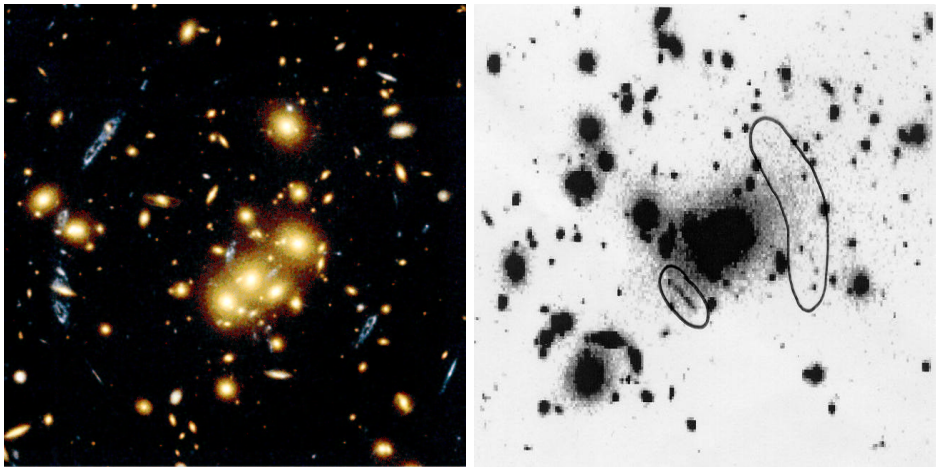

Figure 1.10: *Strong lensing of CL0024+1654 (left) (HST, 1996) and A2219 (right).*

Differentiating equation 1.6 we can express the deformation with the magnification matrix A, which defines the convergence κ and the shear components γ_1 and

γ_2. The isotropic component κ is directly related to the projected mass density, $\Sigma(\theta)$, and γ_1 and γ_2 describes an anisotropic deformation produced by the tidal gravitational field.

$$\frac{d\beta}{d\theta} = A(d\theta) \tag{1.8}$$

$$A = \begin{pmatrix} 1-\kappa-\gamma_1 & -\gamma_2 \\ -\gamma_2 & 1-\kappa+\gamma_1 \end{pmatrix} \tag{1.9}$$

The eigenvalues of the magnification matrix, $1-\kappa \pm |\gamma|$, where $|\gamma| = \sqrt{\gamma_1^2+\gamma_2^2}$, provide the elongation and orientation produced by the gravitational field of the lens on the images of the sources. The magnification of an image is

$$\mu = \frac{1}{det(A)} = \frac{1}{(1-\kappa)^2 - |\gamma|^2}. \tag{1.10}$$

The shapes of faint galaxies can be expressed by their weighted second central moments

$$M_{ij} = \frac{\int S(\theta)(\theta_i - \theta_i^g)(\theta_j - \theta_j^g)d^2\theta}{\int S(\theta)d^2\theta}, \tag{1.11}$$

where the subscipts i and j denote the coordinates and θ^g is the center coordinate. $S(\theta)$ is the surface brightness. Gravitational lensing does not affect the surface brightness of the source. If one assumes that the magnification is constant across the image, the relation between the shape of the source, M^S, and the lensed image, M^I, is

$$M^I = A^{-1}M^S A^{-1}. \tag{1.12}$$

The gravitational lensing transforms a circular source into an ellipse. Its axis ratio is given by the ratio of the two eigenvalues of the magnification matrix. The shape of the lensed galaxies can thus provide information about the shear and the convergence of the gravitational field and thru this give us the projected mass density (Mellier, 1999).

Strong lensing is often a single multiple-image source, while weak lensing deals with the distortion of galaxy shapes, magnification of galaxies and number density effects that are so small ($\kappa \ll 1$ and $|\gamma| \ll 1$) that they cannot be detected on individual objects.

When dealing with the weak lensing of a galaxy cluster we look for a non-zero systematic average of equation 1.11, descibing the shapes of the background galaxies assuming that they have a certain intrinsic statistical distribution. When the light from the background galaxies passes the cluster it is bent and when it reaches us the shape of the galaxies looks different from how they would have looked if the light had not passed the cluster. The statistical distribution of galaxies in our image can give us information about the mass distribution of the cluster. Of course including both dark and luminous matter.

Strong lensing and measurements of rotation curves (see section 1.1) can be used to study dark matter haloes at relatively small radii, while the weak lensing

signal can be measured over large projected distances. This enables us to study the amount of dark matter and the extent and shape of the halo. CDM models predict flat galactic dark matter haloes and investigations using weak lensing have excluded spherical haloes at the 99 % confidence level (Hoekstra et al., 2002). Statistical properties of the galaxy and dark matter distributions provide important constraints on models of galaxy formation and by studying the cosmic shear, which is weak lensing of large scale structure, constraints can be put on cosmological parameters.

The main difficulty associated with detection of matter through weak lensing, is that the distortions of the galaxy shapes are very small, less than a few percent on angular scale, and only detectable statistically. Only rich clusters give a strong enough signal-to-noise ratio. Poorer clusters and individual galaxies will not give a significant detection, but Kaiser & Squires (1993) suggest that by stacking the estimates of Σ for a collection of similar objects one can hope to measure the ensemble average mass profile. Even when observing a very rich cluster the seeing has to be good in order to be sure that the shapes measured are accurate.

2

Observations and Analysis

2.1 Abell 2219

A2219 is a rich cluster at z=0.225 (Allen et al., 1992). Its co-ordinates are RA=16h 40m 21.1s and Dec.=+46d 41m 16s (J2000). It is one of the brightest X-ray clusters detected by the ROSAT All Sky Survey, with a X-ray luminosity of $L_M = 1.8 \cdot 10^{45}$ ergs s^{-1} in the 0.1-2.4 keV band and $L_X = 3.8 \cdot 10^{45}$ ergs s^{-1} in the 2-10 keV band (Bèzecourt et al., 2000), suggesting a high galaxy density.

The cluster shows both weak and strong lensing, with two multiple image systems at different redshift (Gray et al., 2000).

Gray et al. studied the gravitational depletion effect around A2219 using infrared data obtained with CIRSI (Cambridge Infrared Survey Instrument) at the prime focus of the 4.2 m William Herschel Telescope. They estimate the Einstein radius (equation 1.7) of the cluster $\theta_E = 13.7^{+3.9}_{-4.2}$ arcsec with a 66% confidence limit, resulting in a velocity dispersion of $\sigma_v = 814^{+100}_{-86}$ km s^{-1}.

Bézecourt et al. (2000) combined strong and weak lensing observations in optical and near infrared to obtain a mass model and concluded that the total mass of A2219 within 1 Mpc is $8.3 \cdot 10^{14}$ solar masses. They also did a distorsion profile from measurements of the distorsions of the shapes of background galaxies, excluding cluster members. They found that the distorsion profile is consistent with a singular isothermal sphere, with a velocity dispersion of 1075 ± 100 km s^{-1}.

2.2 Observations of Abell 2219

The images I have used were taken by Tomas Dahlén at NOT during the night of June 15 1999, with the Andalucia Faint Object Spectrograph, the Alfosc instrument. The images are CCD images in the I-band. The central wavelength of the I-band is 900 nm and the bandwidth is 240 nm. Each pixel corresponds to 0.189 arcsec and the seeing was 0.80 arcsec.

The total exposure time was 9000 s, divided into 30×300 s exposures. The telescope was dithered 10 arcsec between exposures to reduce flatfield errors. It

was also turned 90 degrees between each two exposures to easier detect bad pixels.

In addition, 11 bias frames and 8 flatfield images were taken. The flatfield was constructed from the 8 twilight images after removing the stars by hand. Each of the 30 cluster images, as well as the images of the standard stars were corrected for flatfield and bias.

The I-band images show a fringe pattern caused by radiation processes in the upper atmosphere. The pattern is weak compared to the stars and galaxies in the cluster images. By removing all objects above a certain pixel value, for each cluster image and then assembling it to one image, a fringe frame was created. The fringe frame was subtracted from each of the 30 cluster images and from the images of the standard stars as well, after adjusting it to the exposure time of the standard frames.

Bad pixels and cosmic rays were removed by hand. The cluster images were aligned, trimmed, corrected for airmass and finally assembled into one image. The final image shown in figure 2.1 has an area of approximately 338"×339".

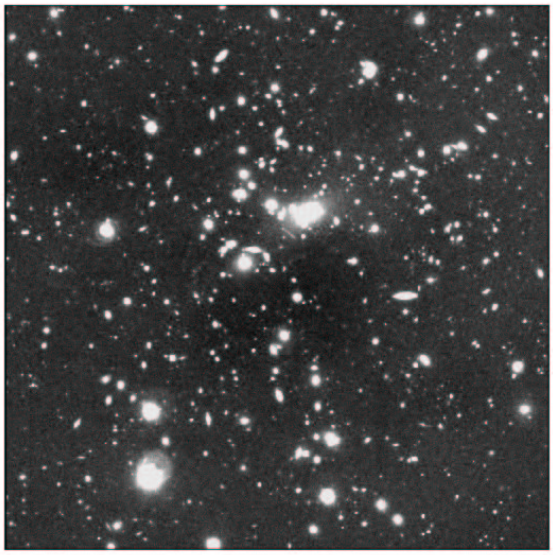

Figure 2.1: *The final image of A2219.*

Standard stars from Landolt (1992) were used to calibrate the photometry.

IRAF (Image Reduction and Analysis Facility) was used to do the image reduction and then FOCAS (Faint Object Classification and Analysis System) (Valdes, 1989) implemented under IRAF for the photometry and creation of the object catalogue.

Foreground stars down to $m_I = 19$ were removed from the object catalogue, checking the FWHM and ellipticities to rule out galaxies.

2.3 Central Galaxy Density

To be able to compare and give some comments to the different luminosity functions in section 3.1 and also to be able to compare A2219 to other clusters, the average central galaxy density, N_r, was calculated for the four clusters in the comparison, A2219, Cl0016+16, Cl1601+42 and MS1008-1224. N_r is defined as the number of bright galaxies ($m \leq m_3 + 3$) projected within a radius r of the brightest cluster galaxy, after correction for background (see section 2.4 for details about the background correction). r was calculated using the following equation:

$$r = d_A \theta, \tag{2.1}$$

where d_A is the angular size distance and θ is the angle (in radians) r subtends on the sky. Ned Wright's Javascript Cosmology Calculator (Ned Wrights Javascript Cosmological Calculator, 2003) was used to calculate the angular size distance for all four clusters.

cluster	z	d_A
A2219	0.225	745.4 Mpc
Cl0016+16	0.546	1317.6 Mpc
Cl1601+42	0.539	1309.1 Mpc
MS1008-1224	0.306	931.4 Mpc

Table 2.1: Redshift (z) and angular size distance (d_A) for the clusters compared.

m_3 is defined as the third brightest galaxy in the cluster and $m_3 + 3$ was chosen as a magnitude limit since it gave fractional uncertainties smaller than 0.5 for all radii and clusters compared. m_3 is known to be dependent on the richness of the cluster. Therefore a magnitude-richness correction is applied to the density counts. To get the right count, N_r^c, N_r was multiplied by the correction factor f_c (Bahcall, 1981). The second column of table 2.2 shows $N_{0.5}$ and the forth column gives the corrected values $N_{0.5}^c$, where r is given in Mpc. The big uncertainty for the value for A2219 is due to lack of data at radius larger than 471 kpc.

It is clear that A2219 is the richest cluster, which is also indicated by the high X-ray luminosity mentioned in 2.1.

Columns 5, 6 and 7 give the corresponding values for 700 kpc and $m_3 + 2$ for Cl0016+16 and Cl1601+42, respectively. Column 7 can be directly compared to $N_{0.5}^{c\,d}$ in table 1 in the article by Bahcall (Bahcall, 1981), to give a larger picture. $N_{0.7}^c$ was only calculated for the clusters Cl0016+16 and Cl1601+42 since $N_r \propto \sigma r^2$ only when $0.1 \leq r \leq 0.5$ Mpc and data was avaliable at these radii only for these two clusters. The errors are Poisson and field-to-field fluctuations from the background counts as described in section 2.4. There are additional errors, both from the distance calculations and from the magnitude limit at m_3+3. An uncertainty in the magnitude limit of ± 0.05 is included in the errors in tables 2.2 and 2.3.

Table 3 shows number of galaxies per kpc^2 for different radii for A2219. It clearly shows the decrease in density with radius.

cluster	$N_{0.5}$	f_c	$N^c_{0.5}$	$N_{0.7}$	f_c	$N^c_{0.7}$
A2219	102 ± 31	1	102 ± 31			
Cl0016+16	84 ± 5	0.91	76 ± 5	34 ± 9	0.73	25 ± 7
Cl1601+42	52 ± 8	0.82	43 ± 7	31 ± 6	0.70	22 ± 4
MS1008-1224	45 ± 5	0.79	36 ± 4			

Table 2.2: Number of galaxies projected within different radii for the clusters.

radius in kpc	no. of galaxies 10^{-4}/kpc^2
0-100	3.03 ± 0.63
100-200	1.86 ± 0.22
200-300	1.24 ± 0.07
300-400	1.16 ± 0.06

Table 2.3: Number of galaxies per kpc^2 for different radii of A2219

Figure 2.2 shows the different circles corresponding to the radii in table 2.3 drawn in the image of A2219.

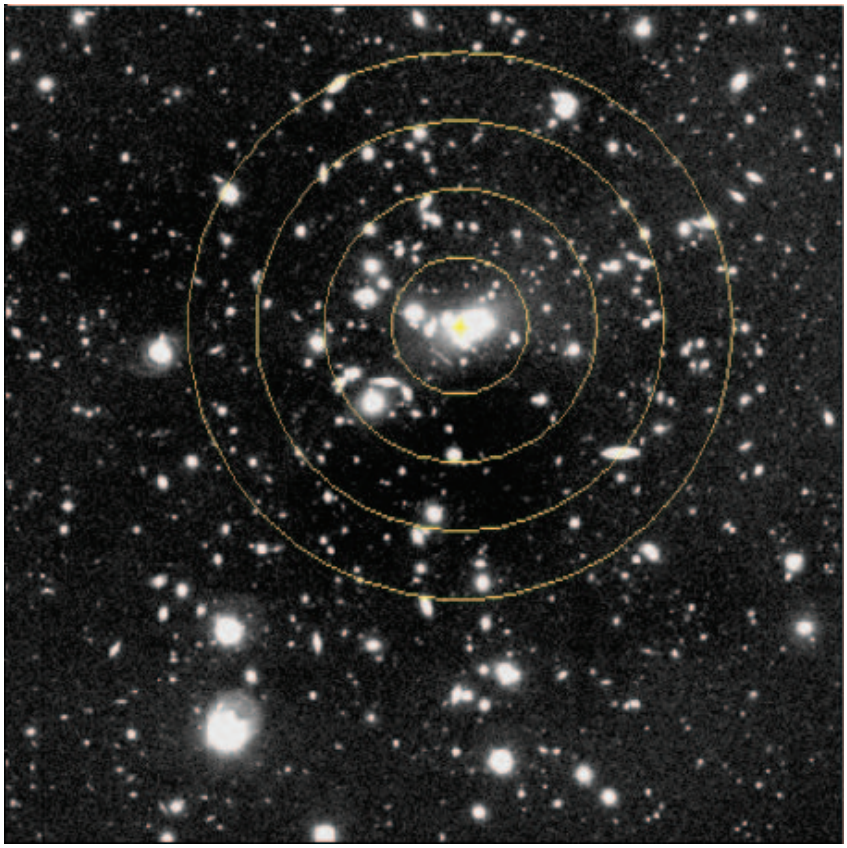

Figure 2.2: *The circles correspond to 100, 200, 300 and 400 kpc from the brightest galaxy in A2219.*

2.4 The Luminosity Function of Abell 2219

In section 1.3 some of the difficulties involved with determining the LF for a cluster was mentioned. The perhaps most important one is to isolate the galaxies that really belong to the cluster from the foreground and background galaxies. The ideal way would be to measure the redshift of all galaxies in a sample and thus be able to pick out the ones in the redshift-range of the cluster. This is, as mentioned above, difficult at high redshifts and faint magnitudes.

Another way, known as photometric redshifts, is to take images in different wavelength bands and by comparing these with a set of galaxy templates at different redshifts obtaining a crude estimate of the redshift.

Because images in only one colour was at hand, a statistical subtraction method-was used to determine the LF of A2219. Counts from a field, preferably nearby the cluster, is subtracted from the field containing the cluster. To make the fields comparable, the counts are binned into half or whole magnitudes and divided by the area of the respective images in degrees. There are some difficulties with this method. One is the Poisson fluctuations. When the background field is subtracted from the image of the cluster, the Poissonian fluctuations in the background field counts affect the resulting number of galaxies in the cluster. When photometric redshifts are avaliable the background subtraction can be limited to a certain redshift range, which obviously decreases the uncertainties in the counts compared to using the full range of redshifts. Another source of uncertainty is the field-to-field variation of our field of view due to the large scale structures of the universe. This is expected to be $\sim$15 % and was included in the calculation of the errorbars in figure 2.4 and 2.5 together with the Poisson fluctuations.

Also, the calibration of magnitudes from standard stars may not be exactly the same for the background field as for the cluster. This too can result in an incorrect counts for the cluster, since the counts are binned in magnitude.

Dahlén et al. (2001) compared background subtraction limited by photometric redshifts to the standard subtraction method and found that the standard method, used here, works reasonably well to redshifts z $\sim$ 0.55, which includes all four clusters in sections 2.3 and 3.1.

Photometry was done on the composite image of A2219 using FOCAS implemented under IRAF, thus attaining the apparent magnitudes and position of the different objects. The apparent magnitudes are isophote magnitudes. The counts of the cluster image and the background, binned in half magnitudes, are shown in figure 2.3.

Absolute magnitudes are calculated from

$$M_R = m_I - DM - K(z), \tag{2.2}$$

where K(z) $=0.44 \pm 0.01$ is the K-correction for the I-band at z=0.225 calculated from the E to Im galaxy templates published by Coleman, Wu and Weedman (1980), DM is the distance modulus and m_I and M_R is the apparent magnitudes in the I-band and the absolute magnitudes in the R-band respectively. Absolute magnitudes are calculated in the R-band since the observed I-band falls on the rest

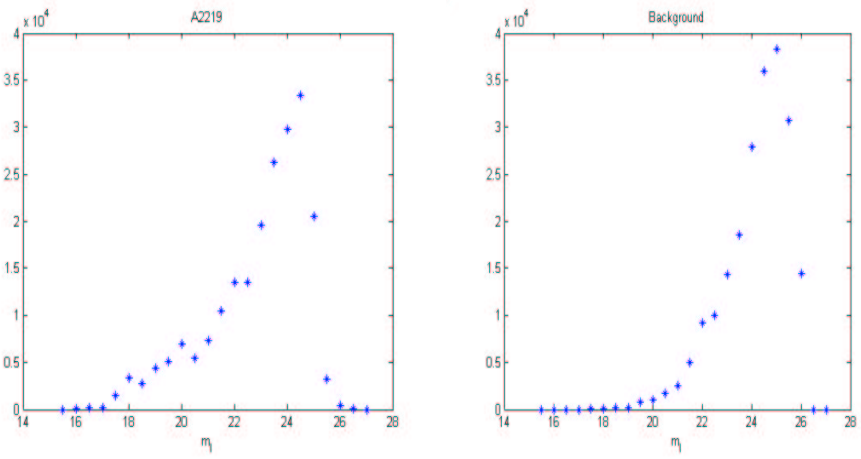

Figure 2.3: *The counts of the cluster field (left) and the background field (right).*

frame R-band at the cluster redshift, making the K-corrections fairly independent on galaxy type.

Figure 2.4 shows the LF of A2219 binned in half magnitudes and figure 2.5 shows it binned in whole magnitudes. The error bars are Poisson and field-to-field fluctuations calculated from the background counts. As can be seen in figure 2.3 the number of counts in the background field starts to increase at m_I ~21 and reaches a peak around m_I ~25. This increase is the reason for the larger error bars for fainter objects, since the size of the errors depend on the background counts. The reason for the completeness limit at M_R=-16 is the different depths of the background and the cluster image (see figure 2.3), as they were taken at different occations and under different conditions and also the limitation of the telescope.

The solid curve in both figure 2.4 and figure 2.5 is a Schechter function as given in section 1.3 (see equation 1.3). The results of the subtractions are adjusted with a least square fit. In section 1.3 the discussions around the validity of the Schechter function are somewhat mentioned. In the case of A2219 it is well fitted for the faint counts. The Schechter function parameters are given in table 2.4.

binsize	α	**M***
0.5 mag	$-1.08^{+0.01}_{-0.10}$	-22.6 ± 0.1
1 mag	$-1.08^{+0.26}_{-0.11}$	-22.4 ± 0.2

Table 2.4: The parameters of the Schechter function fitted to the LF of A2219 in figure 2.4 and 2.5 for different binsizes.

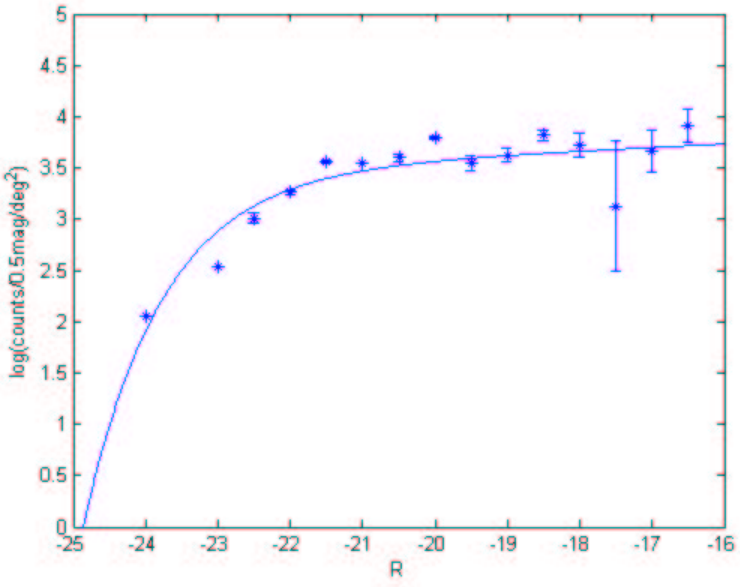

Figure 2.4: *The luminosity function of A2219 binned in half magnitudes.*

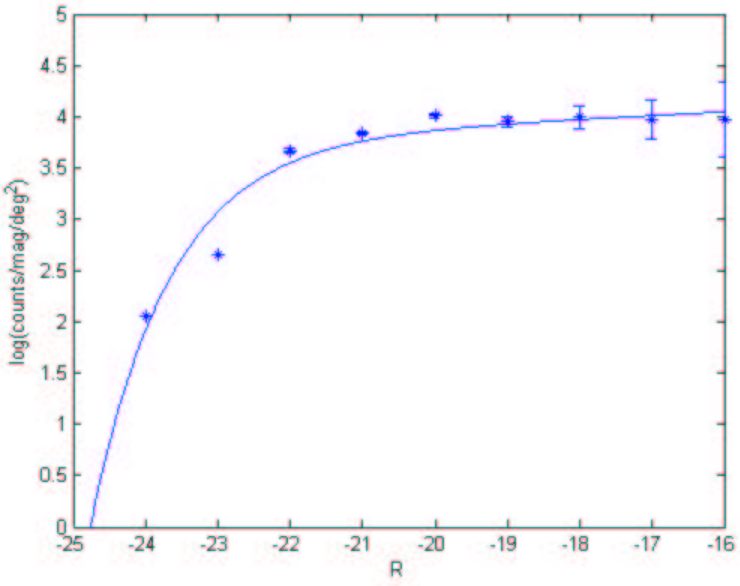

Figure 2.5: *The luminosity function of A2219 binned in whole magnitudes.*

2.5 The Mass Distribution of Abell 2219

To obtain the massmap of A2219 the imcat package (Kaiser et al., 1995) was used. Imcat is a program developed by Nick Kaiser at The Institute for Astronomy at the University of Hawaii. The program uses the ellipticities and positions of the galaxies to calculate the massmap.

Imcats hierarchical object detector, with a 4.5 σ significance threshold, was used first. The object finder gives a crude estimate of the radius and luminosity of each object. This is used as indata for the photometry function. This determines the half-light-radius and total magnitude within an aperture by calculating the growth curve for the integrated light as a function of radius, using the surface brightness corrected for the local background.

To determine the shape of the object imcat contains a function that calculates weighted quadrupole moments:

$$Q_{ij} \equiv \int d^2\theta W(\theta)\theta_i\theta_j S(\theta), \tag{2.3}$$

where angles are measured relative to the object position as determined in the detection phase and $S(\theta)$ denotes the surface brightness. Imcat takes the weight function W(θ) to be Gaussian with scale length equal to a multiple of the aperture radius determined in the object detection phase. The polarization parameters are then defined by:

$$e_\alpha \equiv Q_\alpha / T \tag{2.4}$$

with

$$Q_1 \equiv Q_{11} - Q_{22}, Q_2 \equiv 2Q_{21}, T \equiv Q_{11} + Q_{22}. \tag{2.5}$$

See equation 1.11.

The function that calculates the massmap uses the ellipticities and position vectors from the catalogue to map the mass distribution in the cluster.

$$\Sigma(\theta) = \frac{1}{n} \sum_{galaxies} W(\theta^g - \theta)\chi_i(\theta^g - \theta)e_i(\theta^g), \tag{2.6}$$

where n is the surface number density of background galaxies, W is a weight function and $\chi_i(\theta^g - \theta)e_i(\theta^g)$ is (minus) the tangential alignment of the galaxy at θ relative to the point θ^g, which is the center of the galaxy. For a more detailed description see (Kaiser & Squires, 1993).

First determination of the massmap for the whole image (figure 2.1) was tried, but difficulties arose due to false detections around the foreground stars in the lower left part of the image. Limitation of the catalogue both in magnitude and half-light-radius was tried, but the program had made many small detections around the star and these distorted the massmap image. Finally the image was cut and since imcat requires square images, the massmap is based on a 228" $\times$228" image.

Stars were removed from the object catalogue used to calculate the mass distribution by limiting it, again, in half-light-radius (rh) and magnitude (mag). Figure 2.6 shows apparent magnitudes plotted against half-light-radius for the objects

before and after the stars were removed. The stars are the vertical branch at approximately rh = 2 in the right plot in figure 2.6. The catalogue used to calculate the mass distribution shown in figure 2.7 contains 476 objects. This illustrates some of the difficulties in attaining the mass distribution of a galaxy cluster, especially considering that the LF is based on 1826 objects, including background.

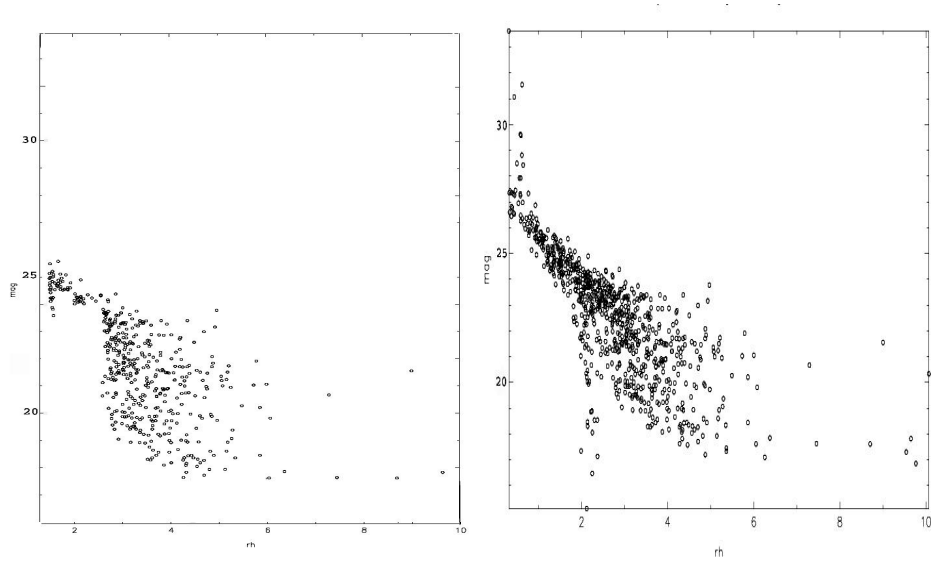

Figure 2.6: *The objects included in the calculation of the massmap (left) and the total number of objects in the image (right).*

The massmap shown in figure 2.7 is scaled in signal to noise. 50 random clusters were simulated from the counts of A2219, massmaps were made on them, they were squared, added together, divided by 50 and the square root was calculated to construct a noise map. Then mean noise was calculated from the noise map and the original massmap was divided by this value.

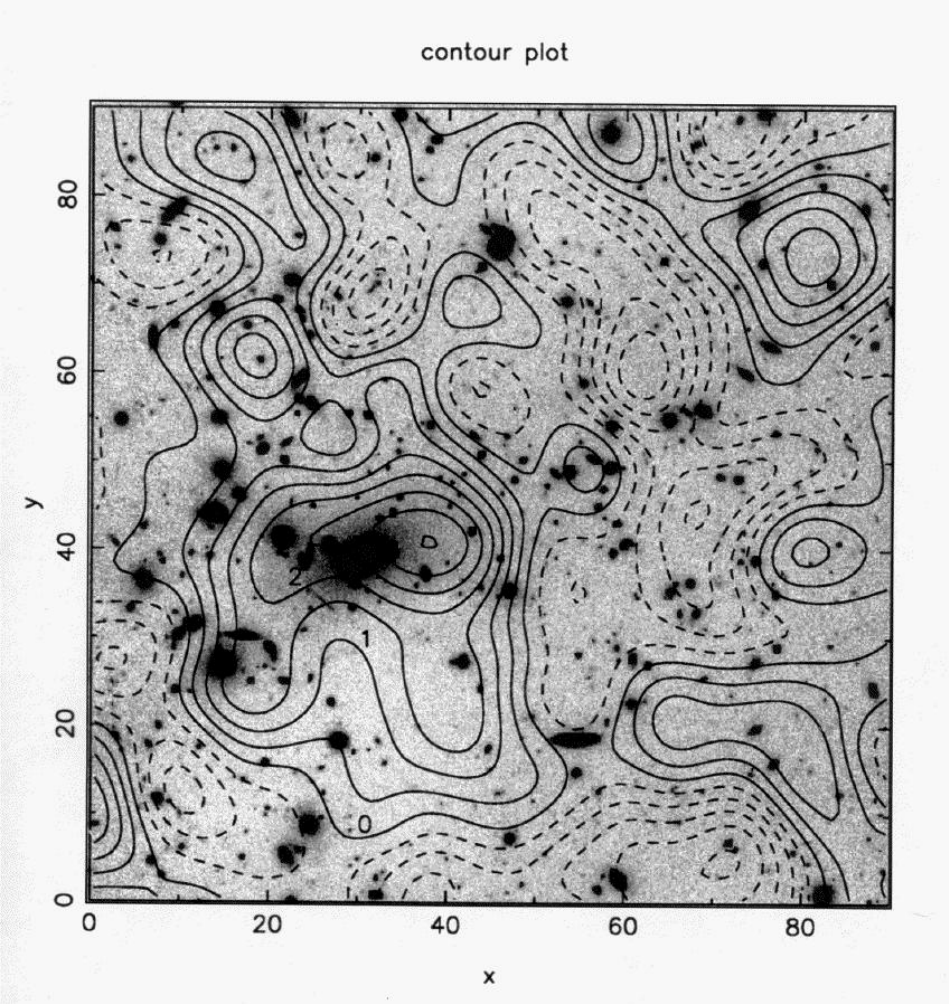

Figure 2.7: *The mass distribution of A2219*

3

Discussion

3.1 The Luminosity Function

In this section the LF of A2219 will be compared with other LFs in order to try and look for correlations. The LFs of the three galaxy clusters Cl0016+16, Cl1601+42 and MS1008-1224 were calculated in the same way as the LF of A2219 (see section 2.4), from catalogues with apparent magnitudes and position. The same subtraction method was used, but with a R-band background field.

Cl0016+16 and Cl1601+42 were observed at NOT by Tomas Dahlén and Magnus Näslund along with background fields, both in the R- and I-bands, used for the background subtraction of all four clusters in figure 3.1 and figure 3.2. The seeing in the images varies between 0.70¨ and 1.15¨.

The observations of MS1008-1224 were carried out by the Science Verification Team at ESO using FORS at the VLT. The seeing in the final frame is 0.65¨. Further details can be found at the ESO web site (ESO, 2003).

All images were reduced using the IRAF package. The absolute magnitudes were all calculated by equation (2.2) using the values in table 3.1.

cluster	**redshift**	**distance modulus**	$\mathbf{K_{xy}}$
A2219	0.225	40.26	$K_{IR} = 0.44$
Cl0016+16	0.546	42.49	$K_{RB} = 0.45$
Cl1601+42	0.539	42.46	$K_{RB} = 0.45$
MS1008-1224	0.306	41.01	$K_{RV} = 0.25$

Table 3.1: Values used to calculate absolute magnitudes for the different LFs.

Two other LFs, here called CZ (Christlein & Zabludoff, 2003) and TT (Trentham & Tully, 2002), were also included in this comparison, both are composite LFs of six different galaxy clusters respectively.

A comparison of the central galaxy densities, as given in section 2.3, X-ray luminosities and velocity dispersions, along with observed area is given in table 3.2.

The values for Cl0016+16, Cl1601+42 and MS1008-1224 are from table 3 in Dahlén et al. (2002), hereafter D02.

cluster	Observed area sq. arcmin	$N^c_{0.5}$	L_X 10^{44} erg s^{-1}	σ km s^{-1}
A2219	31.8	102 ± 31	18^a	1075 ± 100
Cl0016+16	32.5	76 ± 4	34.7^b	1703
Cl1601+42	30.4	43 ± 5	2.1^b	1166
MS1008-1224	32.4	36 ± 3	5.8^b	1054

[a] 0.1-2.4 keV
[b] 0.3-3.5 keV

Table 3.2: Observed area, central galaxy density, X-ray luminosity and velocity dispersion of four galaxy clusters.

The results from the Schechter fits are given in table 3.3. The errors are from the uncertainty in the fits. Additional errors induced by uncertainties in the calculations of absolute magnitude, from the uncertainties in the K-corrections, are not included. The LFs of A2219, Cl0016+16, Cl1601+42 and MS1008-1224 are shown in figure 3.1 and figure 3.2. In figure 3.1 (right) and in figure 3.2, the LF of A2219 is shown as open circles together with the LFs of the other clusters. However, the LF of A2219 is still in R-magnitudes, since the K-corrections are dependent on galaxy type and the different types of the galaxies are unknown. Since the K-corrections are dependent on galaxy type, the shape of a LF is different in different bands. This introduces an uncertainty, when comparing LFs in different restframe bands, as done here.

As a comparison, the LFs of Cl0016+16, Cl1601+42 and MS1008-1224 from D02 are given in figure 3.3. These LFs are the results of calculations using photometric redshifts. The left column shows the total LFs in the rest-frame B-band and the right shows late-type (filled circles) and early-type (open circles) galaxies separately. The division between late-type and early-type is based on spectral type determined by the photometric colors of the galaxies. The first category consists of late-type spirals and irregulars, with a possible inclusion of blue elliptical systems. The second category includes early-type galaxies with red colors, mostly ellipticals and lenticulars, but also passive red spirals.

3.1.1 Cl0016+16

Cl0016+16, at z=0.546, has the highest velocity dispersion in this sample and a high X-ray luminosity. This indicates a high dynamical age. The cluster also has an unusually high fraction of red galaxies compared to other clusters at high redshift (Koo, 1981) and the cluster is thought to be old, despite its high redshift. D02 argue that different dynamical states of a high-z cluster is reflected by the different shapes of the LF. Dynamically older clusters at high redshift should according to

this have LFs similar to local clusters. This is supported by the similarity between the LFs of Cl0016+16 and the Coma cluster (D02).

The high fraction of post-starburst galaxies in Cl0016+16 is also an indication of its high age. The hierarchical clustering scenario predicts a higher fraction of blue galaxies at high z. Kauffmann (1995) finds a difference in the time a rich cluster assembles, depending on redshift. High-z clusters assemble over a shorter time interval. This helps us understand how Cl0016+16 could have a high dynamical age, despite its high redshift.

D02 suggests that the number of field galaxies around Cl0016+16 is depleted by the formation of the supercluster structure that Cl0016+16 is part of. This also explains the large fraction of red galaxies.

3.1.2 Cl1601+42

While the LF of Cl0016+16 is a bit surprising, Cl1601+42, at z=0.539, has a LF that shows features more in accordance with what to expect from a hierachical clustering scenario for a rich cluster at intermediate redshift. The LF of Cl1601+42 differs from that of Coma in a way that indicates that Cl1601+42 is dynamically younger (D02). The LF of Cl1601+42 increases over the whole magnitude range and apparently lacks the plateau at brighter magnitudes seen in the LFs of older clusters. If the cluster has more active starformation, as dynamically younger clusters generally have, there would be a brightening of the faintest cluster members, giving a LF where the curves describing spiral, SO and elliptical galaxies (see figure 1.7) are not apparent.

D02 shows that the steep blue end of the LF of this cluster consists almost exclusively of late-type galaxies, suggested to be recently accreted field galaxies. They also show an increasing fraction of late-type galaxies in the outer parts of the cluster together with a rising blue fraction at large radii, also supporting the accretion scenario.

3.1.3 MS1008-1224

Cl1601+42 and MS1008-1224, at z=0.306, have similar LFs at the faint end, since both clusters have a numerous population of faint late-type galaxies. In the LF of MS1008-1224 this population starts to dominate at a fainter magnitude than for Cl1601+42, resulting in a LF with both plateau and a steep faint end. This is what to expect from a cluster with an intermediate dynamical age. The accretion and starformation is somewhat lesser than in Cl1601+42, but slightly higher than in the dynamically older clusters like Cl0016+16 and Coma.

D02 shows that the fraction of dIrrs in the faint population of MS1008-1224 is higher than in clusters at lower redshift. They suggest that galaxy harassment transforms the faint population so that dEs dominate at lower redshift. D02 also finds that MS1008-1224, as Cl1601+42, has a radial colour gradient much steeper than local clusters.

3.1.4 A2219

The LF of A2219 is, in this comparison, most similar to the LF of MS1008-1224, as could be expected from hierarchical clustering, since they both have low redshift compared to the other clusters (z=0.225 for A2219 and z=0.306 for MS1008-1224). Since they have low redshift, their LFs also go deeper in magnitude.

The plateau in the LF of A2219 is not as apparent as in the LF of MS1008-1224, which is a bit surprising since A2219 has a lower redshift and thus would be expected to be dynamically older. Smail et al. (1995) suggests that the misalignment between the X-ray emitting gas and the mass distribution of A2219 (see next section) indicate that a recent merger event has occured in the cluster. This could lead to an increase in the star formation activity and a general brightening, and perhaps offer one explanation to the apparent lack of a plateau.

A2219 has the highest central galaxy density perhaps indicating a young dynamical age. However, further investigations giving galaxy type would be necessary to establish this.

cluster	redshift	α	M^*	M^*_R
A2219	0.225	$-1.08^{+0.01}_{-0.10}$	-22.6±0.1	-22.6±0.1
MS1008-1224	0.306	$-1.35^{+0.02}_{-0.04}$	-22.7±0.1	-23.2±0.1
Cl1601+42	0.539	$-1.15^{+0.45}_{-0.15}$	-22.3±0.5	-23.8±0.5
Cl0016+16	0.546	$-1.87^{+0.01}_{-0.03}$	-23.2±0.8	-24.7±0.8
CZ	$4000 \leq cz \leq 20000 kms^{-1}$	$-1.21^{0.08}_{-0.07}$	-21.14	-21.14
TT		-1.19 ± 0.03		

Table 3.3: Comparison of the different LFs. α and M* is calculated in the R-band for A2219, CZ and TT, the B-band for Cl0016+16 and Cl1601+42 and the V-band for MS1008-1224. The last column shown M^*_R for all clusters. This is possible by assuming that the brightest galaxies are ellipticals and using the colour difference for elliptical galaxies to calculate M^*_R from M*.

It is apparent that different investigations give different results of α, mostly depending on what kind of fits that were made. Therefore it is important to be careful when making this kind of comparison.

All clusters, except Cl0016+16, which has the highest velocity dispersion, have faint end slopes, α, flatter than the galaxy mass function expected from CDM theory, in agreement with Trentham and Tully (2002) (see section 1.3). The Schechter function of Cl0016+16 in this fit does not fully show the curvature of the LF. A different fit, like the one made by D02 (see figure 3.3), with a separation between different galaxy types, will give a different α. D02 did a straight line fit to the five faintest bins resulting in $\alpha = 0.65 \pm 0.10$ for Cl0016+16, which is much flatter than the galaxy mass function.

Again with one exception, this time of Cl1601+42, there is an apparent correlation between increase in redshift and increase in LF slope at the faint end. This is expected if smaller galaxies merge into larger ones as time passes. Again, this

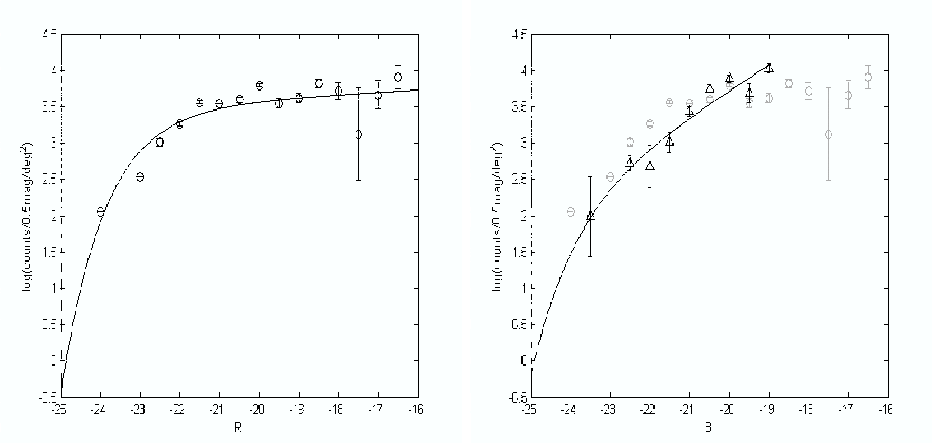

Figure 3.1: *The LFs of A2219 (left) and Cl0016+16 (right).*

depends on what kind of fits that were made. D02 gets different results depending on how the LF is limited in magnitude.

There is no evidence for decrease in the number of faint galaxies with increase in central galaxy density, again with a reservation for the uncertainty of the correlation between α and the actual number of faint galaxies. Neither is the universal luminosity function for clusters is supported by this investigation (compare row 2-5 to row 6 and 7 in table 3.3). An universal LF would indicate a low rate of morphological evolution in galaxy clusters.

Further investigation of the LF of A2219, using photometric redshifts or even spectroscopy to establish galaxy type and making different fits, using both Schechter and Gaussian functions, would give a clearer picture of the dynamical state of the cluster. Giving both opportunity to further investigate the age of the cluster and perhaps confirming the suggested merger event. The suggested investigation would also explain the not so apparent plateau in comparison to MS1008-1224 at higher redshift.

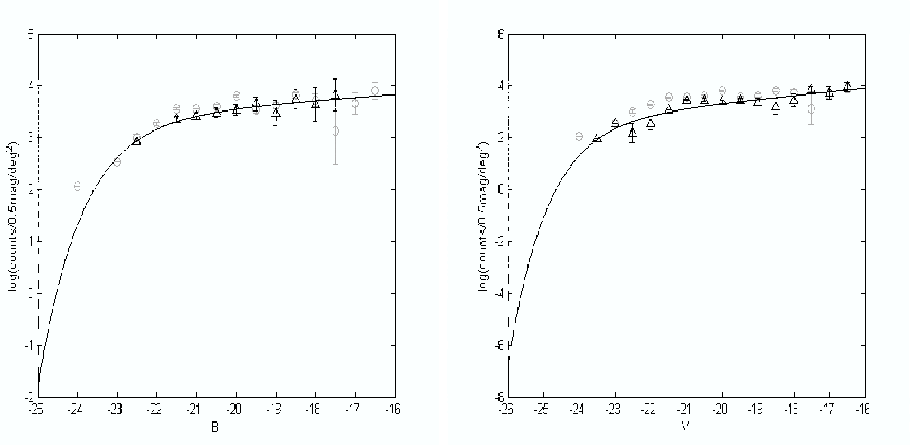

Figure 3.2: *The LFs of Cl1601+42 (left) and MS1008-1224 (right).*

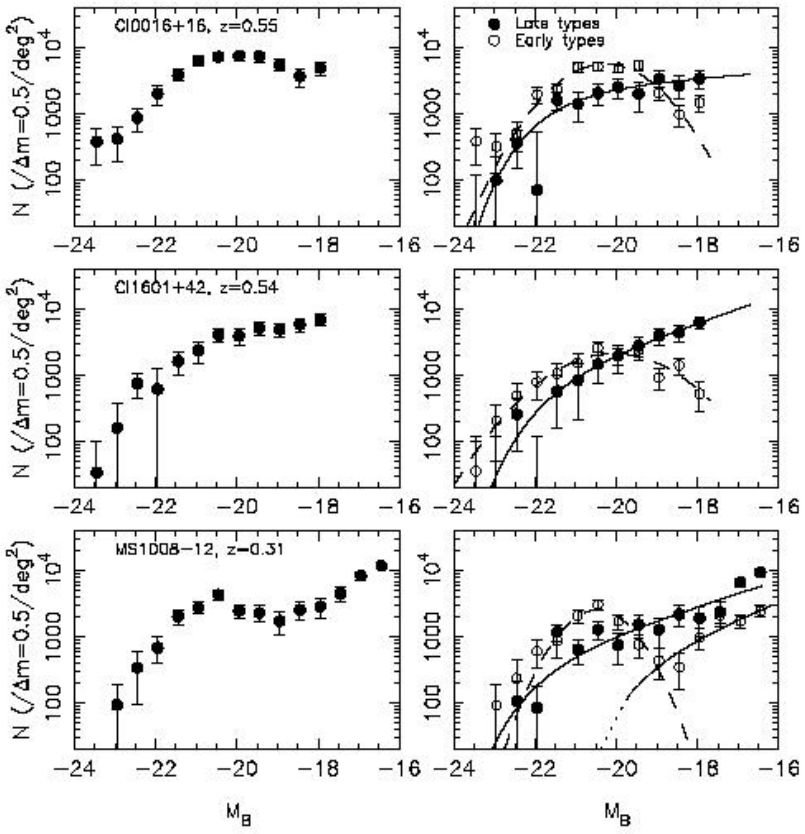

Figure 3.3: *The LFs of Cl0016+16, Cl1601+42 and MS1008-1224 according to Dahlén et al. (2002).*

3.2 The Mass Distribution

The mass distribution of the central part of A2219 has mass peaks that coincide rather well with the luminosity distribution. The most prominent peak is close to the central concentration of galaxies, centered at the cD galaxy at x≈30 and y≈40, in the image of A2219 from this investigation, figure 3.4. The mass peaks both to the upper left (x≈20 and y≈60, hereafter UL) and lower left (x≈20 and y≈25, hereafter LL), as well as the small peak at the upper right (x≈55 and y≈50, hereafter UR) agrees well with the presence of several galaxies. The contours to the lower right of the central cD (x≈40 and y≈20) contradicts the lack of galaxies in this part of the cluster. The contours here are, however, uncertain since the contour labeled 1 corresponds to S/N=1. This means that the signal and noise level are equal at the contour.

A closer look at the mass distribution shows that the highest peak is not exactly centered at the central cD, but slightly to the right, indicating a discrepancy between the distribution of luminous matter and dark matter. This may suggest that the cluster is not fully relaxed in the dark matter potential.

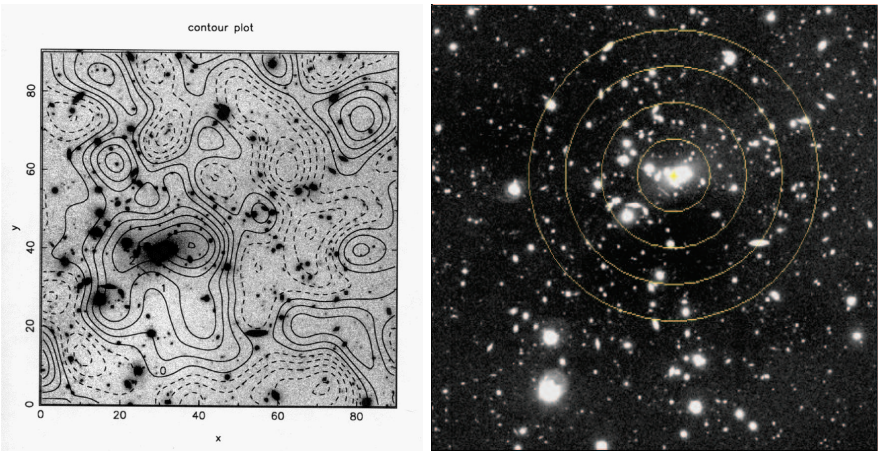

Figure 3.4: *The left figure shows the mass distribution of A2219 according to this investigation. The right figure shows A2219 with circles corresponding to different distances (100, 200, 300 and 400 kpc) from the brightest galaxy.*

The mass distribution also agrees well with the galaxy number density given in section 2.3. A comparison between the massmap to the left in figure 3.4 and the circles in the image to the right, together with table 3.4, shows that the decline in the number density with increasing radius agrees well with the massmap contours.

Figure 3.5 shows the weak lensing massmap of A2219 by Bèzecourt et al. (2000) (B00), calculated using the imcat software. The whole massmap agrees rather well with the results from this investigation. Most of the most significant peaks coincide. In particular, the offset of the central peak was also found by B00. When using

radius in kpc	no. of galaxies 10^{-4}/kpc^2
0-100	3.03 ± 0.05
100-200	1.86 ± 0.05
200-300	1.24 ± 0.05
300-400	1.16 ± 0.05

Table 3.4: Number of galaxies per kpc^2 for different radii of A2219

the software, I found it very sensitive to small changes in the parameters set and to how the object detection was made. Small false detections around removed stars, for instance, forced a cut in the image used to make the massmap, as mentioned in section 2.5. This probably is the reason for the differences between the weak lensing massmap from B00 and the massmap of this investigation. One difference is that B00 used a significance threshold of 4 σ above the local sky background in the object detection, while this investigation used a threshold of 4.5 σ. Another is of course the different quality of the observations, since weak lensing investigations uses faint objects.

Another difficulty when dealing with weak lensing is atmospheric seeing. Due to atmospheric turbulence, a point-like source will be seen from the ground as an extended image. In the image reduction the image was corrected for airmass. Imcat contains a function that calculates and compensates for the point-spread-function for all objects in a catalogue. It uses a catalogue of objects, rejecting objects with large ellipticities (like galaxies). I tried this function, using the whole catalogue of A2219 as input, and it made no difference in the resulting massmap. Thus, this function was not used when calculating the final mass distribution shown in figure 3.4. Perhaps if I had created an image containing only stars, the result would have been different. B00 used another method, instead of imcat, to correct for the PSF. The PSF correction could be another reason for the differences between the massmap of this investigation and that of B00.

B00 also calculated the central mass distribution of A2219 with two different methods using the strong lensing of the cluster and different simulations. One of their resulting massmaps is shown in figure 3.6. Again the peaks coincides rather well with the massmap derived in this investigation. This time, however, with the most significant peak at the center of the central cD galaxy. The peak LL agrees well with this investigation as does UL and UR.

Smail et al. (1995) compared the morphology of the X-ray map and the mass distribution of A2219 and found that the major axis of the X-ray gas is misaligned with the major axis inferred from the mass distribution and and with the galaxy distribution. They found a deviation of 13 degrees, which clearly is higher than their estimated error of 4 degrees. When comparing figure 3.4 with figure 3.7 we see a similar discrepancy. Smail et al. (1995) notes that the major axis of the X-ray emission lies close to the direction between the central cD and a compact group of galaxies to the lower left of the cD (x$\approx$15 and y$\approx$30). They suggest that the cluster is undergoing, or has recently undergone, a core-penetrating merger, as the

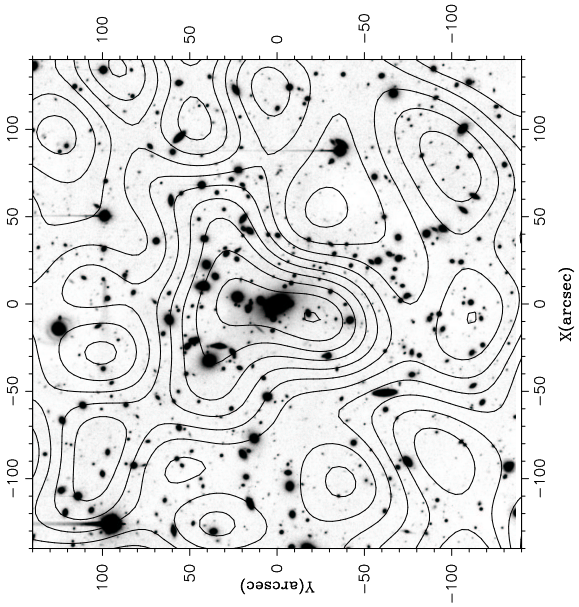

Figure 3.5: *The mass distribution inferred from weak lensing of A2219 according to Bèzecourt et al. (2000).*

merging group would inject kinetic energy into the cluster gas along the merger axis.

Further investigations of A2219, including the redshift distribution, would enable an investigation where the background galaxies can be separated from the cluster galaxies. By removing the cluster galaxies from the images, errors in the mapping of the mass distribution could be avoided. This would give answers to whether the cluster is dynamically relaxed or not and make it easier to find out the dynamical state of the cluster, also considering the possible ongoing merger.

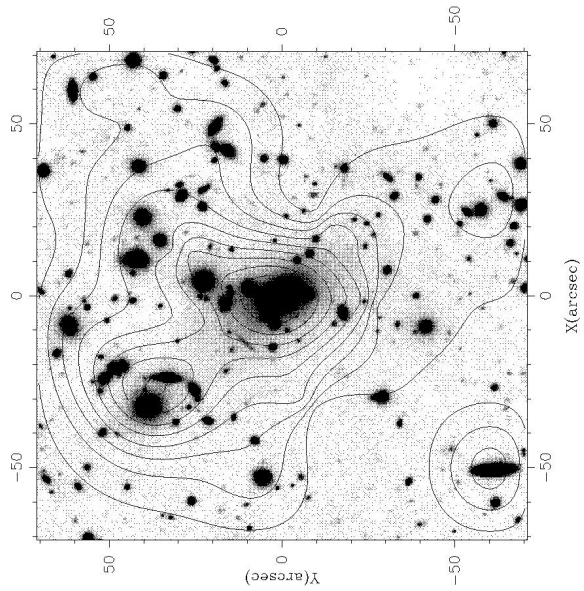

Figure 3.6: *The mass distribution inferred from strong lensing of A2219 according to Bèzecourt et al. (2000).*

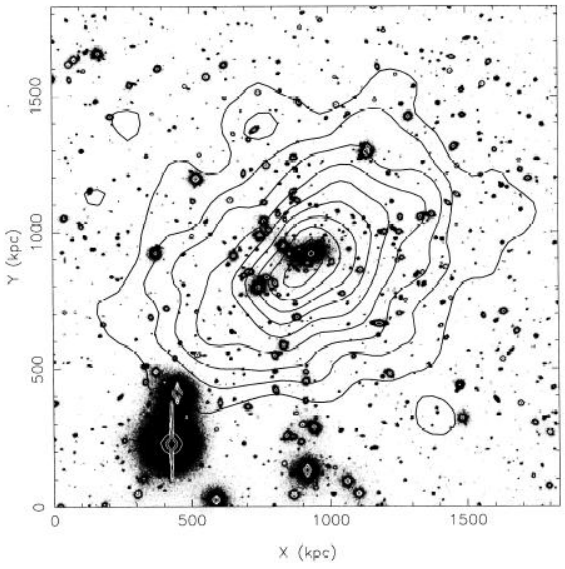

Figure 3.7: *An I image of A2219 showing the distribution of bright galaxies in the central part of the cluster. Overlayed is the ROSAT HRI exposure, smoothed with a 140 kpc FWHM Gaussian.*

4

Summary and conclusions

Images taken at NOT of the galaxy cluster A2219 were analyzed, resulting in a LF and a massmap showing the projected mass density.

The LF was compared to LFs of other clusters, and the LF of A2219 was found to be most similar to the cluster that is closest in redshift (MS1008-1224), consistent with the hierachical clustering scenario. The LF also shows a younger dynamical age of A2219, compared to MS1008-1224, although the latter has a higher redshift. Different explanations are suggested.

A more general conclusion is that most clusters, in this comparison, have faint end slopes flatter than the galaxy mass function according to CDM theory. This does not contradict CDM theory. It only suggests that not all matter is visible. The faint end of the LF of galaxy clusters can give us a lot of information about the structure of the universe and the evolution of galaxy clusters. If smaller galaxies merge into larger ones, the number of faint galaxies will increase with redshift, as in this investigation. No evidence for a decrease in the number of faint galaxies with an increase in central galaxy density was found. An universal luminosity function for clusters is not supported by this investigation.

The projected mass density is consistent with other investigations of A2219, and there is a discrepancy between the position of the center of the luminous and the dark matter. Also there is a misalignment between the mass distribution and major axis of the X-ray emission, confirming earlier results.

Further investigations, using both LFs and weak lensing, together with, for instance, X-ray maps, of a well-defined sample of rich clusters would help us to better understand the role of mergers in clusters and give clarity to the processes governing growth and evolution of structure in the universe.

Acknowledgements

I would like to thank Claes Fransson for his advice and for helping me finding the right articles, Tomas Dahlén for his never-ending patience, Margrete Wold for helping me understand weak lensing and Magnus Näslund.

I would also like to thank my brother, David Bergström for helping me with LaTeX despite his own tight schedule trying to finish his PhD-thesis.

Bibliography

S. W. Allen et al.: Optical spectroscopy of the ROSAT X-ray brightest clusters, MNRAS, 259, 67, 1992.

A. Babul & M. J. Rees: On dwarf elliptical galaxies and the faint blue counts, MNRAS, 255, 346, 1992.

A. Babul & H. C. Ferguson: Faint blue galaxies and the epoch of dwarf galaxy formation, ApJ, 458, 100, 1996.

N. A. Bahcall: The relation between velocity dispersion and central galaxy density in clusters of galaxies, ApJ, 247, 787, 1981.

J. E. Barnes & L. Hernquist: Transformations of galaxies. II. Gasdynamics in merging disk galaxies, ApJ, 471, 115, 1996.

M. Bartelmann & P. Schneider: Weak gravitational lensing, astro-ph/9912508, 1999.

C. L. Bennett et al.: First year Wilkinson Microwave Anisotropy Probe (WMAP) observations: Maps and basic results, ApJ, submitted.

J. Bèzecourt et al.: Strong and weak lensing analysis of cluster Abell 2219 based on optical and near infrared data, Astronomy and Astrophysics, astro-ph/0001513, 2000

B. Binggeli et al.: The luminosity function of galaxies, ARA&A, 26, 509, 1988.

J. Binney & S. Tremaine: Galactic dynamics, Princeton University Press, 1987.

D. Christlein & A. I. Zabludoff: Galaxy luminosity functions from deep spectroscopic samples of rich clusters, astro-ph/0304031 v1, 2003.

J. M. Colberg et al.: Clustering of galaxy clusters in CDM universes, MNRAS, 000, 1, 2000.

G. D. Coleman et al., ApJS, 43, 393, 1980.

T. Dahlén et al.: The galaxy population of Cl1601+42 at z=0.54, MNRAS, 000, 1, 2001.

T. Dahlén et al.: The galaxy population of intermediate redshift clusters, submitted to MNRAS, 2002.

A. Diaferio et al.: The spatial and kinematic distributions of cluster galaxies in a LCDM universe–Comparison with observations, MNRAS, in press 2001.

S. P. Driver & A. Fernàndez-Soto: Dwarfmology, astro-ph/9805100, May 1998.

S. P. Driver et al.: Luminosity distributions within rich clusters-III: A comparative study of seven Abell/ACO clusters, MNRAS, 301, 369, September 1998.

J. Dubinski: The origin of the brightest cluster galaxies, ApJ, 502, 141, July 1998.

ESO homepage: http://www.eso.org/science/ut1sv/Clus_index.html, 2003.

C. S. Frenk et al.: Physica Scripta, T36, 70, 1991.

C. S. Frenk et al.: Galaxy formation and evolution: What to expect from hierarchical clustering models, 1996.

M. E. Gray et al.: Infrared observations of gravitational lensing in Abell 2219 with CIRSI, MNRAS, in press 2000.

J. S. Heyl et al.: Galaxy formation in a variaty of hierachical models, MNRAS, 274, 755, 1995.

H. Hoekstra et al.: Current status of weak gravitational lensing, New Astronomy Reviews, 46, 767, 2002.

J. P. Huchra et al.: A deep Abell cluster redshift survey, ApJ, 365, 66, 1990.

Hubble Space Telescope Press Release, 1996.

Hubble Space Telescope Press Release, 1997.

N. Kaiser & G. Squires: Mapping the dark matter with weak gravitational lensing, ApJ, 404, 441, 1993.

N. Kaiser et al.: A method for weak lensing observations, ApJ, 449, 460, 1995.

G. Kauffmann: Hierachical clustering and the Butcher-Oemler effect, MNRAS, 274, 153, 1995.

D. C. Koo: Multicolor photometry of the red cluster 0016+16 at z=0.54, ApJ, 251, L75, 1981.

Landolt A. U., AJ, 104, 340, 1992.

H. Lin et al. : The power spectrum of galaxy clustering in the Las Campanas Redshift Survey, ApJ, 471, 617.

E. Linder, SNAP Collaboration: Revealing dark energy with the next generations of supernovae surveys, American Astronomical Society Meeting 201, 2002.

Y. Mellier: Cosmological applications of gravitational lensing, astro-ph/9901116, 1999.

B. Moore et al.: On the survival and destruction of spiral galaxies in clusters, MNRAS, 304, 465, 1999.

S. Perlmutter & E. Linder: Overview of supernova cosmology to Date, 2002.

S. Phillipps et al.: Environmental effects on the faint end of the luminosity function, astro-ph/9812229, 1998.

F. Schweizer: Colliding and merging galaxies, Science, 231, 227-234, January 1986.

M. Serano: Probing the dark energy with strong lensing by clusters of galaxies, Astronomy and Astrophysics, v. 393, 757, 2002.

I. Smail et al.: The discovery of two giant arcs in the rich cluster A2219 with the Keck telescope, MNRAS, 277, 1, 1995.

A. Toomre & J. Toomre: Galactic bridges and tails, ApJ, 178, 623, December 1972.

N. Trentham: The dwarf galaxy population of the Coma cluster to MR = -11 -A detailed description, MNRAS 293, 71, 1998.

N. Trentham & R. B. Tully: The faint end of the galaxy luminosity function, MNRAS, 335, 712, 2002.

R. B. Tully et al.: Squelched galaxies and dark halos, ApJ, 569, 573, 2002.

M. S. Turner: Dark Energy and the new cosmology.

J. A. Tyson: Deep CCD survey: Galaxy luminosity and color evolution, AJ, 96, 1, 1988.

F. Valdes: Faint Object Classification and Analysis System, NOAO, Tucson, AZ, October 1982 & F. Valdes: Faint Object Classification and Analysis System standard test image results, NOAO, Tucson, AZ, 1989.

S. D. M. White & C. S. Frenk: Galaxy formation through hierarchal clustering, ApJ, 379, 52, 1991.

http://www.astro.ucla.edu/ wright/CosmoCalc.html, 2003.

List of Figures